Journal of Nuclear Materials 405 (2010) 95–100

Contents lists available at ScienceDirect

Journal of Nuclear Materials

journal homepage: www.elsevier.com/locate/jnucmat

Tensile properties and deformation mechanisms of a 14Cr ODS ferritic steel

A. Steckmeyer [a,*], M. Praud [a], B. Fournier [a], J. Malaplate [a], J. Garnier [a], J.L. Béchade [a], I. Tournié [a], A. Tancray [a], A. Bougault [a], P. Bonnaillie [b]

[a] Service de Recherches Métallurgiques Appliquées, CEA Saclay, Gif-sur-Yvette, France
[b] Service de Recherche en Métallurgie Physique, CEA Saclay, Gif-sur-Yvette, France

ARTICLE INFO

Article history:
Received 15 March 2010
Accepted 20 July 2010

ABSTRACT

The search for a new cladding material is part of the research studies carried out at CEA to develop a sodium-cooled fast reactor meeting the expectations of the Generation IV International Forum. In this study, the tensile properties of a ferritic oxide dispersion strengthened steel produced by hot extrusion at CEA have been evaluated. They prove the studied alloy to be as resistant as and more ductile than the other nano-reinforced alloys of literature. The effects of the strain rate and temperature on the total plastic strain of the material remind of diffusion phenomena. Intergranular damage and intergranular decohesion are clearly highlighted.

1. Introduction

The high interest for oxide dispersion strengthened (ODS) ferritic steels in the field of nuclear energy, and particularly as cladding material, is mainly due to their excellent resistance to both irradiation swelling [1] and high-temperature creep [2–6]. The body-centered cubic structure of the ferritic matrix is responsible for the former property while the latter is widely attributed to the fine dispersion of oxide particles – or nanoclusters [7]. Along with ODS martensitic steels, which show the same two properties, ODS ferritic steels are one of the most promising solutions to meet the specifications for the fuel cladding material for future generations of fission nuclear plants.

The want for improvement in safety, energetic efficiency and sustainability for future nuclear systems lead to high-demanding specifications concerning the fuel claddings. The objective of long-term availability of the nuclear fuel implies to raise its combustion rate as much as possible. This means the fuel claddings will have to be kept inside the reactor as long as possible and thus to undergo a very high irradiation dose: 200 dpa. To improve the energetic efficiency of the plant, the operating temperature will be raised up to 650 °C, compared to the 350 °C of many existing pressurized water reactors. Due to this high temperature and due to the gas released from the fuel pellets during the nuclear reaction, the main solicitation of the claddings will be internal pressure creep. The approximate hoop stress value should be 100 MPa by the end of life. The resilience, fracture toughness and ductility of the cladding material at lower temperature are also expected to be sufficient to provide a high degree of safety during maintenance operations.

In this study, the tensile properties of an ODS ferritic steel containing 14% by weight of chromium and produced at the CEA are presented. This alloy is designated as J05. It was hot extruded in the form of bars and did not undergo any subsequent recrystallisation heat treatment. Its mechanical properties along the extrusion direction are evaluated from room temperature to 750 °C. They prove the J05 to be among the best ODS steels of literature, especially concerning high temperature ductility. The influence of the strain rate on the mechanical behaviour is also studied, as well as the evolution of the strain localisation in the necking. Post-mortem observations are conducted to study the deformation mechanisms. Since the material production route was stopped way before the final tubular structure, the mechanical results of the present study do not represent exactly the mechanical properties of an ODS cladding tube. A change in the grain size, the grain morphology, the dislocations density and the crystallographic texture is expected. Of course, mechanical tests on thin tubes are much more tricky and difficult to perform. However, the present work enables to improve the knowledge of the relationship between microstructure, mechanical properties and deformation and damage mechanisms of ODS steels.

2. Experimental procedures

2.1. Manufacturing process

The J05 ODS steel has the following nominal composition (in wt.%): Fe–14Cr–1W–0.26Ti–0.3Y_2O_3. Its actual composition, measured by ICP-AES (inductively coupled plasma atomic emission spectroscopy) is given in Table 1. The material was produced by

* Corresponding author. Tel.: +33 1 6908 1211; fax: +33 1 6908 7130.
E-mail address: antonin.steckmeyer@cea.fr (A. Steckmeyer).

0022-3115/$ - see front matter © 2010 Elsevier B.V. All rights reserved.
doi:10.1016/j.jnucmat.2010.07.027

Table 1
Composition (in wt.%) of the J05 steel. Measures were made by ICP-AES.

Fe	Cr	W	Ti	Y	O	C	Si	Ni	Mn
–	13.65	1.17	0.30	0.26	0.06	0.05	0.27	0.16	0.33

mechanically alloying a pre-alloyed metal powder and an yttria powder. This step was done by the Austrian company *Plansee*. The resulting powder, with a granulometry finer than 150 μm, was sealed into a mild steel can, degassed at 300 °C, consolidated into a bar by hot extrusion at 1100 °C and then air-cooled. The 16 mm diameter rod produced was then simply annealed at 1050 °C for 1 h and air-cooled.

The homogeneity of the J05 ODS steel bar has been evaluated, through electron probe microanalyses (EPMA) and micro-hardness measures. The mean hardness value under an 0.1 kg load is 434 $HV_{0.1}$, and no heterogeneity was noted, except at the periphery of the bar section where a 10% increase in hardness was detected. In this 2 mm wide area, diffusion of carbon from the mild steel used for canning may have occurred and could be responsible for the observed slight rise of the material hardness.

2.2. Tensile tests

Two specimen geometries have been used to characterise the mechanical properties of the J05 steel in tension. For both type of specimen, the tensile direction was parallel to the longitudinal direction of the extruded bar. The first specimen geometry has an 11.5 mm gauge length and a 2 mm × 2 mm square section. It has been used to follow the strain evolution during testing using an optical camera. The second specimen geometry has a 15 mm gauge length and a 3 mm diameter circular section. Every specimen was machined from the homogeneous part of the ODS steel bar. Tensile tests were carried out in air at temperatures ranging from 25 °C to 750 °C. They were strain controlled with strain rates between 10^{-5} s^{-1} and 5×10^{-2} s^{-1}.

3. Results

3.1. Microstructure

Characterisation of the grain morphology using a transmission electron microscope (TEM) showed the grains were elongated along the extrusion direction (Fig. 1b) and relatively equiaxed in the bar section (Fig. 1a). The mean length of the grains is 1.2 μm, their mean width is about 550 nm and the grain aspect ratio (GAR) is around 2.5. Texture analyses were conducted using both electron back-scattering diffraction (EBSD) and X-ray diffraction (XRD) techniques. They revealed a very strong fibre texture, the preferential crystallographic orientation being ⟨1 1 0⟩ along the extrusion direction, as presented in Fig. 1c. The same measurements conducted on the MA957 ODS steel, produced by *Inco*, showed an almost complete fibre texture, with local reinforcement. The preferential orientation along the extrusion direction was also ⟨1 1 0⟩, but this texture was less pronounced. The results from the EBSD technique on as-received J05 alloy revealed a higher GAR than TEM observations, due to the presence of low-angle boundaries, as seen in Fig. 1d.

Nano-particles have been observed in the material (by TEM) and their size distribution was studied thanks to image analysis. Their mean size and spatial density turn out to be respectively 2.3 nm and 5×10^{22} m^{-3} (which leads to a mean spacing between particles equal to 27 nm). Larger particles were also observed on some grain boundaries. They appear to be aligned along the extrusion direction and their mean size is about 100–200 nm, with a maximum of 1 μm. An energy dispersive X-ray spectroscopy revealed these particles were mainly Ti-rich, the biggest ones being aluminium compounds. Such stringer-like titanium-rich particles were previously reported in ODS steels [8–10].

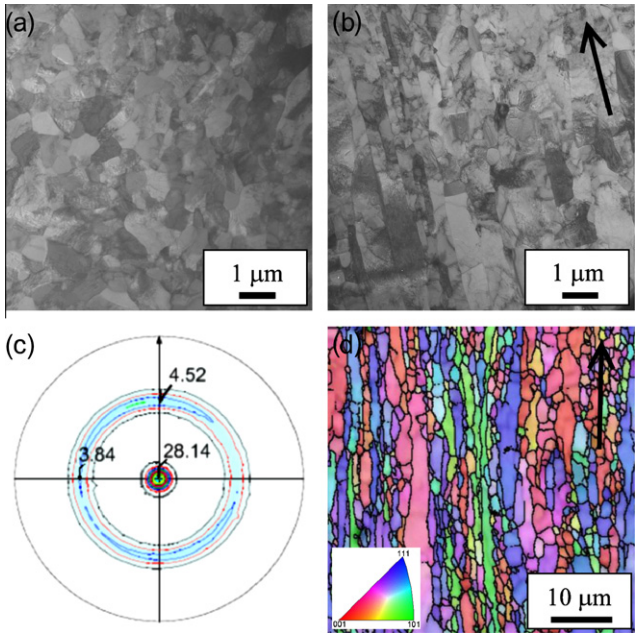

Fig. 1. Description of the as-received microstructure of the J05 ODS alloy. TEM images with an extrusion direction respectively (a) perpendicular to the image plane and (b) along the arrow. ⟨1 1 0⟩ pole figure obtained by XRD (c) and EBSD crystallographic orientation map (d) (extrusion direction is along the arrow).

3.2. Tensile properties

The results concerning the proof strength (measured with an offset of 0.2% plastic strain) and the ultimate tensile strength of the J05 ODS steel are gathered in Fig. 2. They first highlight the very limited strain hardening of this alloy. Indeed, at high strain rates ($\sim 10^{-3}$ s^{-1}), there is less than 10% of strain hardening at room temperature, and this value decreases with temperature down to 1% at 750 °C. The same statement is made at lower strain rates (10^{-5} s^{-1}). The measured values at room temperature are high and typical of nano-reinforced steels: a proof stress of 1080 MPa

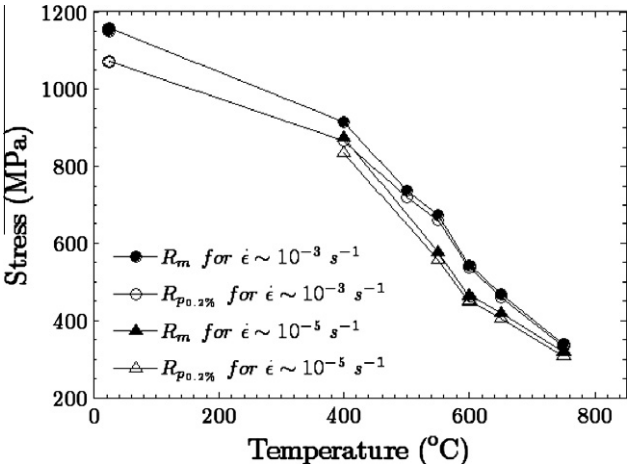

Fig. 2. Temperature and strain rate dependence of the tensile strength and yield stress of J05 steel.

and an ultimate stress of 1150 MPa. At this temperature, no influence of the strain rate was noted between $7 \times 10^{-4}\,s^{-1}$ and $5 \times 10^{-2}\,s^{-1}$. A decrease of the proof and ultimate stresses is observed when the temperature increases. This decrease seems to be more pronounced above 400 °C.

The evolution of the total plastic elongation according to the temperature and strain rate is given in Fig. 3. Between room temperature and 400 °C, the ductility of the material is greater than 20% and is only slightly influenced by the strain rate. Above 400 °C, the evolution of ductility is on the contrary influenced by the strain rate in a strong and less usual manner: the higher the strain rate, the higher the ductility. At 600 °C, the ductility exhibits a peak for all tested strain rates. Therefore, above 600 °C, a lower strain rate and a higher temperature both lead to a reduced ductility. For example, the tensile test carried out at 750 °C and $10^{-5}\,s^{-1}$ fractured at only 3.4% of plastic strain.

The necking coefficient $Z = 100 * (S_{initial} - S_{fracture})/S_{initial}$ measures the relative reduction of the area $S_{fracture}$ of the fracture surface with respect to the initial area $S_{initial}$ of the sample. It was determined with an optical microscope for every specimen. Fig. 4 shows the evolution of this coefficient according to the temperature and strain rate. It appears that Z decreases continuously with the temperature: the higher the temperature, the smaller the Z, i.e. the larger the area of the fracture surface. The necking coefficient is also influenced by the strain rate, in the way that the area of the fracture surface increases with the strain rate. This strain rate effect is relatively reduced at 400 °C and strongly emphasized at higher temperatures. The existence of a maximum of ductility at 600 °C is not clearly correlated to the evolution of Z according to the temperature.

3.3. Evolution of the necking

In order to measure the local strain inside the necking, an optical follow up with a camera was made during the tensile test of some plane samples. From the obtained pictures, it was possible to observe the initiation and evolution of the necking. Bridgman's local stress and strain, which take into account the radius of curvature of the necking area, could then be calculated (see Fig. 5 for the definitions). Even if this technique was first developed for axisymmetric specimen [11], its relevance for squared section tensile specimen has been demonstrated [12,13]. Fig. 6 compares the three tensile curves deduced from the tensile test carried out at 25 °C and $7 \times 10^{-4}\,s^{-1}$: the engineering tensile curve, the true stress/true strain tensile curve and Bridgman's local tensile curve. As long as the necking is small, Bridgman's and true stress/true

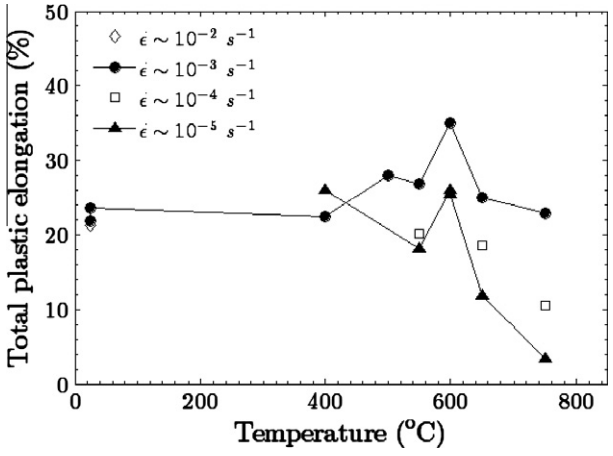

Fig. 3. Temperature and strain rate dependence of the total plastic elongation in tension of J05 steel.

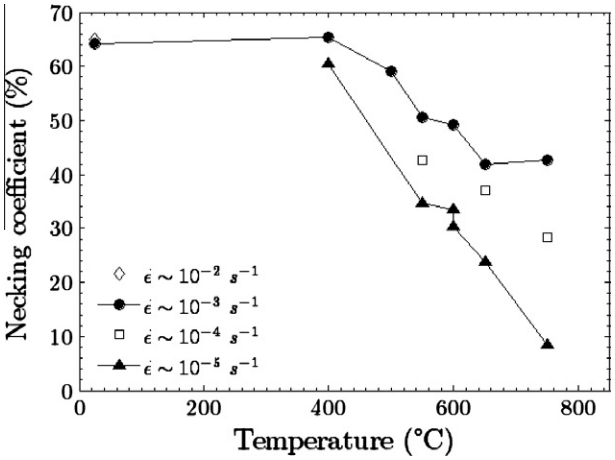

Fig. 4. Temperature and strain rate dependence of the necking coefficient for J05 tensile tests.

$$\varepsilon_{Bridgman} = 2\ln\left(\frac{a_0}{a}\right)$$

$$\sigma_{Bridgman} = \frac{\frac{F}{\pi a^2}}{\left(1+\frac{2R}{a}\right)\ln\left(1+\frac{a}{2R}\right)}$$

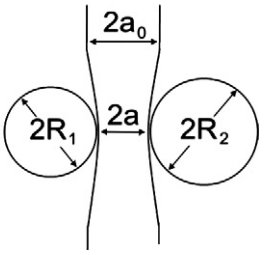

Fig. 5. Definition of Bridgman's local stress and strain, where F is the loading force and R the mean value of R_1 and R_2.

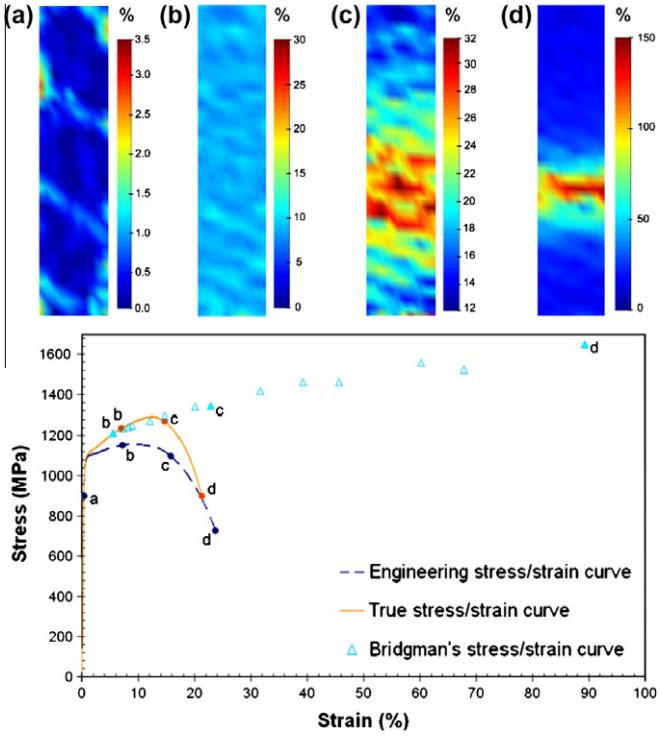

Fig. 6. Comparison of the different tensile curves for a J05 specimen tested at 20 °C and $7 \times 10^{-4}\,s^{-1}$. Bridgman's curve refers to the local behaviour of the necking area. Four strain fields calculated thanks to *Correlmanuv* indicate the evolution of the strain distribution during the test.

strain curves are almost superimposed. These two curves then split apart, which means the necking is no longer negligible compared to the homogeneous reduction of the sample section. The strain at which the split between these two curves occurs turns out to be approximately $\varepsilon_{true}(\sigma_m)$, i.e. the strain for which the true stress/true strain tensile curve reaches its maximum value. This strain value, below which the necking can be neglected, appears to be much higher than $\varepsilon_{ing}(R_m)$, which is the strain corresponding to the maximum of the engineering tensile curve.

The use of the image correlation software *Correlmanuv* enabled to determine non-uniform strain fields. The strain fields corresponding to four different total strain levels are also shown in Fig. 6. They confirm that the strain is almost homogeneous on the gauge length as long as the maximum of true strain is not reached. Consequently, compared to the engineering quantities (stress and strain), the true stress and true strain are more appropriate to describe the mechanical behaviour of the J05 ODS steel tensile tests. This point is of importance given the shape of the engineering tensile curve (exhibiting a very limited hardening combined with a low strain value at the ultimate strength point).

The evolution of the homogeneous plastic strain (the true plastic strain at the maximum of true stress) shows the exact same trend with respect to temperature and strain rate as the total plastic strain (Fig. 2).

4. Discussion

4.1. Mechanical properties

The tensile mechanical properties of the 14Cr ODS steel produced at the CEA are compared to the main ferritic nano-reinforced alloys of literature [4,8,14,15] in Fig. 7. Fig. 7a compares the high strain rate ductility of various ODS steels. It shows that the alloy under study is much more ductile than the others, from room temperature to 800 °C. For example, in this range of temperature, its total elongation is up to twice as important as the one of the 12YWT and 14YWT alloys, studied at the Oak Ridge National Laboratory [4,14]. Fig. 7a also points out that the peak of ductility observed for the J05 alloy at 600 °C is detected for the other alloys too, but at higher temperatures. As for the low strain rate ductility, it could not be compared to literature due to a lack of available data. Up to now, the J05 steel has proved to be a quite ductile ODS steel. Fig. 7b shows that its yield strength lies among the highest values of literature, which is also true for its ultimate strength. Eventually, J05 ODS steel appears less resistant than the 12YWT and 14YWT alloys but however, it exhibits an excellent compromise between strength and ductility.

The underlying application being cladding tubes undergoing internal pressure, the mechanical properties of the J05 ODS steel in the hoop direction should also be studied. To investigate the mechanical anisotropy of the material, tensile tests along transverse and 45° directions will be carried out. Existing results from literature concerning ODS steels demonstrate that the transverse resistance is almost as high as the longitudinal one [16–18] and that, depending on the grade, the transverse ductility can be reduced down to 30% of the longitudinal ductility [16,17]. A degradation of mechanical properties between longitudinal and hoop directions has also been reported for creep tests on the ODS ferritic steel MA957 [19,20].

4.2. Deformation mechanisms

Tensile tests carried out on the J05 ODS steel have shown this alloy was more ductile and more resistant than many pre-existing nano-reinforced alloys. They also pointed out a peak of ductility for this material, at 600 °C. Beyond this temperature, it was observed that both a rise of the temperature and a decrease of the strain rate lead to a reduced total elongation. Such an observation promotes the idea of the existence of a deformation mechanism that would require high temperatures and long time of solicitation to occur and develop. A deformation mechanisms linked to diffusion phenomena is thus suspected.

In order to investigate the suspected change in deformation mechanisms, one can compare the evolution of the yield stress of the J05 steel with the predictions of various strengthening models, as done in [21] for a nickel-base ODS superalloy. Fig. 8 illustrates this comparison. Three different models are considered: (i) a Bailey–Hirsch relationship illustrating the hardening due to dislocations forest ($\sigma_{BH}/M \sim \alpha\mu b\rho^{1/2}$), (ii) the Orowan critical stress as suggested by Kocks [22] (see Eq. (1)) and (iii) a critical stress calculated by Reppich [23] (see Eq. (2)). The latter relationship is based on the Arzt–Rösler–Wilkinson (ARW) model of interfacial pinning which describes the by-passing of dislocations pinned on the departure side of oxide particles [24,25]. In these equations, $M = 2.9$ is the Taylor factor for body-centered cubic polycrystals, $\rho = 10^{14}\ m^{-2}$ is the dislocations density, $L = 27$ nm is the mean spacing between particles, $d_{ox} = 2.3$ nm is the mean diameter of oxides particles, μ is the shear modulus, depending on the temperature, $\nu = 0.3$ is the Poisson's coefficient, $b = 0.25$ nm is the Burger's vector, $\alpha = 0.5$ and $R = 0.77$ quantifies the decrease of line tension of a pinned dislocation segment. The values of the shear modulus

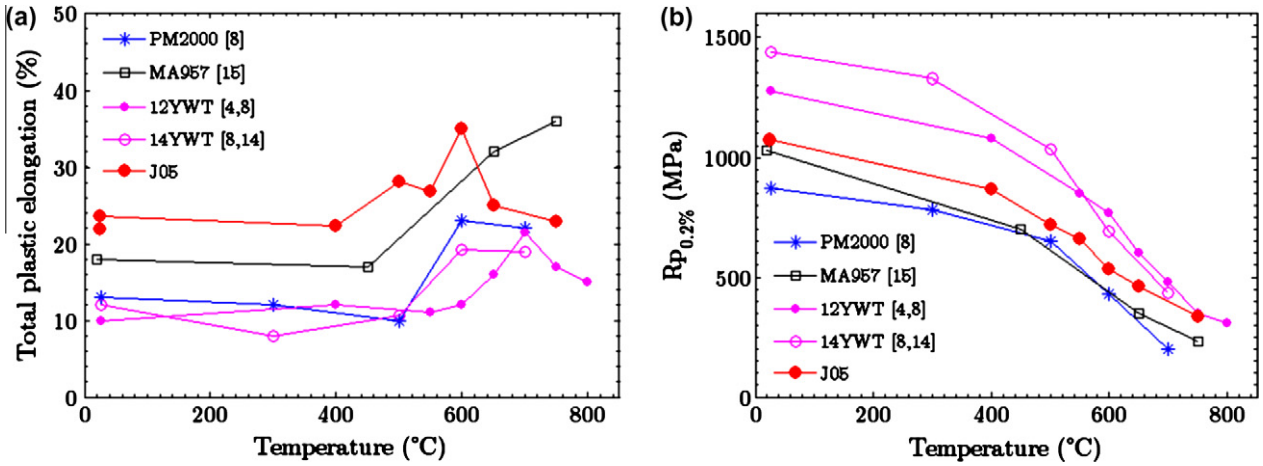

Fig. 7. Temperature dependence of the total plastic strain (a) and yield stress (b) of J05 steel and other ODS ferritic steels of literature.

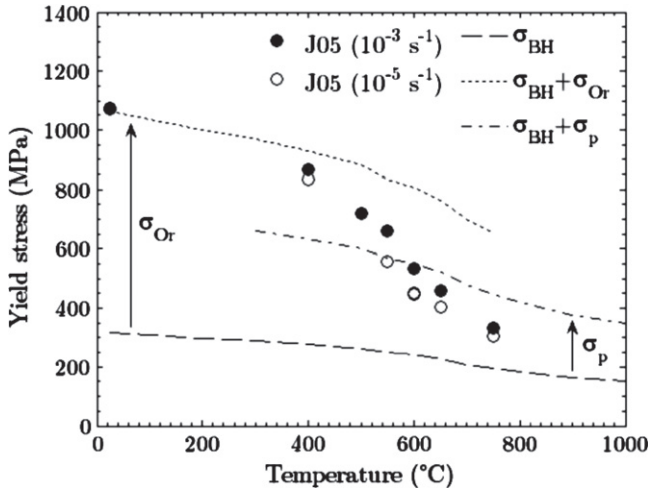

Fig. 8. Modelling of the evolution of the yield stress of J05 ODS steel with temperature. Bailey–Hirsch hardening (σ_{BH}) acts as a baseline. Additional Orowan (σ_{Or}) and ARW (σ_p) hardening mechanisms are assumed respectively at low and high temperatures.

μ used to calculate these yield stress predictions were deduced from ultrasonic measurements of the Young's modulus of the J05 ODS steel, assuming isotropic elasticity: $\mu = E/2(1+\nu)$.

In Fig. 8, Bailey–Hirsch hardening can be considered as the yield strength of a grade of J05 steel without dispersion strengthening. From this figure, it can be seen that taking into account an Orowan hardening in addition to Bailey–Hirsch hardening enables to describe the yield strength of J05 ODS steel from 20 °C to 400 °C. Above 800 °C, replacing Orowan hardening by the ARW model leads to an overestimation of the yield strength. This overestimation may be partly explained by a decrease of Bailey–Hirsch hardening due to the evolution of coefficient α with respect to temperature. This decrease, predicted by Kocks and Mecking [26], is not considered here. However, it appears that the ARW model alone acts as a lower bound very close to J05 experimental data. These results prove Orowan and Arzt–Rösler–Wilkinson mechanisms to be relevant strain mechanisms respectively at low and high temperatures since they partly enable to account for the strength of J05 alloy. However, they do not describe correctly the relatively strong decrease of the yield stress observed between 400 °C and 800 °C. Nor they can account for the dependence of the yield stress towards strain rate because no viscosity or diffusive phenomenon is described by the three previous hardening models. Grain morphology should also be taken into account to describe the anisotropy of the materials properties of extruded ferritic ODS steels. Such a Hall–Petch hardening was suggested by Ratti [27] for an 18Cr ODS steel.

$$\sigma_{or} = 0.9M \frac{[\ln(4[\pi d_{ox}/4]/b)]^{3/2}}{[\ln(L/b)]^{1/2}} \frac{\mu b^2/4\pi(1-\nu)}{b(L-[\pi d_{ox}/4])} \quad (1)$$

$$\sigma_{p} = 0.9M \frac{R^{3/2}}{2\sqrt{2}+R^{3/2}} \frac{\mu b}{L} \quad (2)$$

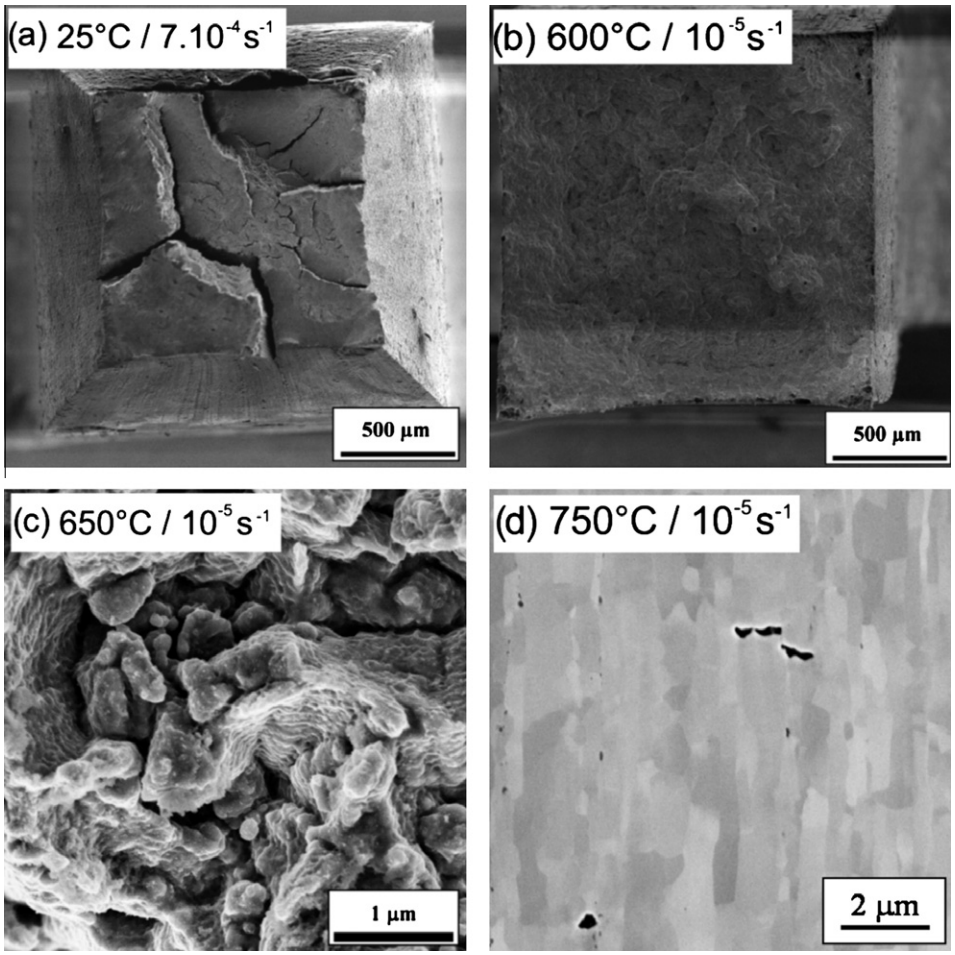

Fig. 9. SEM images of fractured specimens with different testing conditions. Fractured surfaces (a, b and c) and longitudinal cut (d). The loading axis is vertical in (d).

4.3. Fracture surfaces properties and damage

Fracture surfaces corresponding to several strain rates and testing temperatures have been observed. It appears that between room temperature and 400 °C, the fracture surfaces show typical ductile fracture, with well defined dimples. At room temperature, secondary cracks propagating parallel to the tensile axis are noticed (Fig. 9a). With increasing temperature, the number of dimples decreases, and they get smaller. From 600 °C, the fracture surfaces are different (Fig. 9b). Dimples are still observed, but they are located at the periphery of the fracture surfaces. In a central area, a clear intergranular decohesion is noticed. Observations from a scanning electron microscope (SEM) revealed both grains and ligaments of ductile tearing meandering among these grains (Fig. 9c). The lower the strain rate and the higher the testing temperature, the more pronounced the intergranular decohesion. The surface of intergranular decohesion gets larger with increasing temperature and represents up to 40% of the total fracture surface.

The observation of specimens cut along the loading/extrusion direction was also carried out with a SEM. Far from the fracture surface, two types of cavities have been detected (Fig. 9d). The first type gathers cavities located at grain boundaries which are perpendicular to the loading direction. Since the loading direction for all specimens was parallel to the direction of elongation of the grains, these damaged grain boundaries are the ones at the ends of the grains. On the contrary, the second type gathers cavities located along grain boundaries parallel to the loading direction and aligned with the stringer-like Ti-rich particles observed on the as-received material. The growth of those cavities is not a priori promoted by the loading, which underlines the role of the bigger particle on damage mechanisms, as reported in [10].

5. Conclusion

In this work, the tensile properties of the J05 ferritic ODS steel with 14% of chromium are presented for different temperatures and strain rates. This alloy was prepared in the form of bars with a 16 mm diameter and was tested in tension along the extrusion direction. The measured mechanical properties are very promising, compared to other ODS steels. Deformation and damage mechanisms were investigated. The main results are the following:

- The J05 steel exhibits more than 20% of total plastic strain from room temperature to 750 °C and for a strain rate of 10^{-3} s^{-1}. A peak of ductility is reached at 600 °C. J05 lies among the most tensile resistant nano-reinforced steel of literature.
- Above 400 °C, a strain rate effect has been observed: the lower the strain rate, the lower the ductility. This trend is increased at higher temperatures and is in agreement with the low elongation at fracture reported in the literature for longitudinal creep tests on ODS steels.
- The strain localisation as a necking occurs at the maximum of the true stress/true strain tensile curve, which justifies the use of these two quantities rather than the engineering quantities.
- A change of deformation mechanisms with temperature is noticed. A thermally-activated depinning mechanism is suspected above 800 °C while Orowan bowing mechanism is consistent at lower temperatures. A competition between both mechanisms is likely to occur between 400 °C and 800 °C.
- An intergranular decohesion on fractured surfaces has been highlighted. It was observed at temperatures above 400 °C and appeared to intensify at higher temperatures.
- Both grain boundaries parallel and perpendicular to the loading direction were damaged. The presence of 100 nm Ti-rich particles seems to play a major role on the formation and growth of the observed cavities.

The direction of the Nuclear Energy Department of the CEA is acknowledged for financial support through the DISN/TEMAS project.

References

[1] J.J. Huet, Powder Metall. Rep. 40 (1985) 155.
[2] D.K. Mukhopadhyay, F.H. Froes, D.S. Gelles, J. Nucl. Mater. 258 (1998) 1209.
[3] S. Ukai, T. Okuda, M. Fujiwara, T. Kobayashi, S. Mizuta, H. Nakashima, J. Nucl. Sci. Technol. 39 (2002) 872.
[4] R.L. Klueh, P.J. Maziasz, I.S. Kim, L. Heatherly, D.T. Hoelzer, N. Hashimoto, E.A. Kenik, K. Miyahara, J. Nucl. Mater. 307 (2002) 773.
[5] A. Alamo, V. Lambard, X. Averty, M.H. Mathon, J. Nucl. Mater. 329 (204) 333.
[6] T. Hayashi, P.M. Sarosi, J.H. Schneibel, M.J. Mills, Acta Mater. 56 (2008) 1407.
[7] D.T. Hoelzer, J. Bentley, M.A. Sokolov, M.K. Miller, G.R. Odette, M.J. Alinger, J. Nucl. Mater. 367 (2007) 166.
[8] R.L. Klueh, J.P. Shingledecker, R.W. Swindeman, D.T. Hoelzer, J. Nucl. Mater. 341 (2005) 103.
[9] R. Kasada, N. Toda, K. Yutani, H.S. Cho, H. Kishimoto, A. Kimura, J. Nucl. Mater. 367 (2007) 222.
[10] H. Sakasegawa, S. Ohtsuka, S. Ukai, H. Tanigawa, M. Fujiwara, H. Ogiwara, A. Kohyama, Fusion Eng. Des. 81 (2006) 1013.
[11] P.W. Bridgman, Studies in Large Plastic Flow and Fracture, Mcgraw-Hill editors, New York, 1952.
[12] Z.L. Zhang, M. Hauge, J. Odegard, C. Thaulow, Int. J. Sol. Struct. 36 (1999) 3497.
[13] A. Bacha, D. Daniel, H. Klocker, J. Mater. Proc. Technol. 184 (2007) 272.
[14] D.A. McClintock, D.T. Hoelzer, M.A. Sokolov, R.K. Nanstad, J. Nucl. Mater. 386 (2009) 307.
[15] H. Réglé, Ph. D. Thesis, Paris XI University, 1994.
[16] T. Furukawa, S. Ohtsuka, M. Inoue, T. Okuda, F. Abe, S. Ohnuki, T. Fujisawa, A. Kimura, in: Paper 9221 in Proceedings of ICAPP'09, Tokyo, Japan, May 2009.
[17] M.J. Alinger, G.R. Odette, G.E. Lucas, J. Nucl. Mater. 307 (2002) 484.
[18] E. Lucon, Fusion Eng. Des. 61 (2002) 683.
[19] B. Wilshire, T.D. Lieu, Mater. Sci. Eng. A 386 (2004) 81.
[20] M.C. Salston, G.R. Odette, Fusion Materials Semiannual Report, DOE-ER-0313/44, August 2008, p. 62.
[21] M. Nganbe, M. Heilmaier, Mater. Sci. Eng. A 387 (2004) 609.
[22] U.F. Kocks, Mater. Sci. Eng. A 27 (1977) 291.
[23] B. Reppich, Acta Mater. 46 (1998) 61.
[24] E. Arzt, D.S. Wilkinson, Acta Metall. 34 (1986) 1893.
[25] E. Arzt, J. Rösler, Acta Metall. 36 (1988) 1053.
[26] U.F. Kocks, H. Mecking, Prog. Mater. Sci. 48 (2003) 171.
[27] M. Ratti, Ph. D. Thesis, Institut Polytechnique de Grenoble, 2009.